Inorg. Chem. **2008**, *47*, 6040−6050

Inorganic Chemistry
Article

Anionic Roussin's Red Esters (RREs) *syn*-/*anti*-$[Fe(\mu\text{-SEt})(NO)_2]_2^-$: the Critical Role of Thiolate Ligands in Regulating the Transformation of RREs into Dinitrosyl Iron Complexes and the Anionic RREs

Tsai-Te Lu,[†] Chih-Chin Tsou,[†] Hsiao-Wen Huang,[†] I-Jui Hsu,[‡] Jin-Ming Chen,[§] Ting-Shen Kuo,[||] Yu Wang,*[,‡] and Wen-Feng Liaw*[,†]

Department of Chemistry, National Tsing Hua University, Hsinchu 30013, Taiwan, Department of Chemistry, National Taiwan University, Taipei 106, Taiwan, National Synchrotron Radiation Research Center, Hsinchu, Taiwan, and Instrumentation Center, National Taiwan Normal University, Taipei, Taiwan

Received February 27, 2008

The anionic *syn*-/*anti*-$[Fe(\mu\text{-SEt})(NO)_2]_2^-$ (**2a**) were synthesized and characterized by IR, UV−vis, EPR, and X-ray diffraction. The geometry of the $[Fe(\mu\text{-S})_2Fe]$ core is rearranged in going from $[\{Fe(NO)_2\}^9\text{-}\{Fe(NO)_2\}^9]$ Roussin's red ester $[Fe(\mu\text{-SEt})(NO)_2]_2$ (**1a**) (Fe···Fe distance of 2.7080(5) Å) to the $[\{Fe(NO)_2\}^9\text{-}\{Fe(NO)_2\}^{10}]$ complex **2a** (Fe···Fe distance of 2.8413(6) Å) to minimize the degree of Fe···Fe interaction to stabilize complex **2a**. On the basis of X-ray absorption (Fe K- and L-edge), EPR and SQUID, complex **2a** is best described as the anionic $[\{Fe(NO)_2\}^9\text{-}\{Fe(NO)_2\}^{10}]$ Roussin's red ester with the fully delocalized mixed-valence core. The complete bridged-thiolate cleavage yielded DNIC $[(EtS)_2Fe(NO)_2]^-$ (**3a**) in the reaction of 2 equiv of $[EtS]^-$ and complex **1a**, whereas reaction of 2 equiv of $[^tBuS]^-$ with $[Fe(\mu\text{-S}^t\text{Bu})(NO)_2]_2$ (**1b**) gave DNIC $[(^tBuS)_2Fe(NO)_2]^-$ (**3b**) and the anionic Roussin's red ester $[Fe(\mu\text{-S}^t\text{Bu})(NO)_2]_2^-$ (**2b**) through bridged-thiolate cleavage in combination with reduction. In contrast to the inertness of DNIC **3b** toward complex **1b**, nucleophile DNIC **3a** induces the reduction of complex **1a** to produce the anionic Roussin's red ester **2a**. Interestingly, dissolution of complex **3a** in MeOH at 298 K finally led to the formation of a mixture of complexes **2a** and **3a**, in contrast to the dynamic equilibrium of complexes **3b** and **1b** observed in dissolution of complex **3b** in MeOH. These results illustrate the aspect of how the steric structures of nucleophiles ($[EtS]^-$ vs $[^tBuS]^-$ and $[(EtS)_2Fe(NO)_2]^-$ vs $[(^tBuS)_2Fe(NO)_2]^-$) function to determine the reaction products.

Introduction

Dinitrosyl iron complexes (DNICs) are known as one of the two potential naturally occurring forms for storage and delivery of NO in biological systems.[1] NO can be stored in the form of protein-bound DNICs and is probably released from cells in the form of low-molecular-weight DNICs (LMW DNICs).[2] NO release is regulated by the ligands coordinated to the $\{Fe(NO)_2\}$ unit. NO has been demonstrated to react with the Fe−S clusters of several proteins including succinate dehydrogenase,[3a] nitrogenase,[3b] succinate-Q reductase,[4a] mitochondrial aconitase,[4b] cytosolic aconitase,[4b] HiPIP,[4c] endonuclease III,[4d] mammalian ferrochelatase,[4e] and SoxR to form the monomeric, EPR-active DNICs.[4f] As has been known, characterization of both protein-bound DNICs and LMW DNICs in vitro is possible via their distinctive electron paramagnetic resonance (EPR) signals at $g = 2.03$.[1,2] Recently, the protein-bound DNIC

* To whom correspondence should be addressed. E-mail: wfliaw@mx.nthu.edu.tw.
[†] National Tsing Hua University.
[‡] National Taiwan University.
[§] National Synchrotron Radiation Research Center.
[||] National Taiwan Normal University.

(1) (a) Butler, A. R.; Megson, I. L. *Chem. Rev.* **2002**, *102*, 1155–1166. (b) Ueno, T.; Susuki, Y.; Fujii, S.; Vanin, A. F.; Yoshimura, T. *Biochem. Pharmacol.* **2002**, *63*, 485–493. (c) Frederik., A. C.; Wiegant, I. Y.; Malyshev, I. Y.; Kleschyov, A. L.; van Faassen, E.; Vanin, A. F. *FEBS Lett.* **1999**, *455*, 179–182. (d) McCleverty, J. A. *Chem. Rev.* **2004**, *104*, 403–418. (e) Hayton, T. W.; Legzdins, P.; Sharp, W. B. *Chem. Rev.* **2002**, *102*, 935–991.

(2) (a) Mülsch, A.; Mordvintcev, P.; Vanin, A. F.; Busse, R. *FEBS Lett.* **1991**, *294*, 252–256. (b) Cooper, C. E. *Biochim. Biophys. Acta* **1999**, *1411*, 290–309. (c) Foster, M. W.; Cowan, J. A. *J. Am. Chem. Soc.* **1999**, *121*, 4093.

10.1021/ic800360m CCC: $40.75
Published on Web 06/03/2008

was characterized by X-ray crystallography through addition of a dinitrosyldiglutathionyl iron complex into human glutathione transferase P1−1 in vitro/in vivo.[5]

Roussin's red esters (RREs), the dimeric form of DNICs considered to perform the similar role as DNICs, are diamagnetic and EPR-silent because of the antiferromagnetic coupling between the two iron centers.[6] Formation of the protein-bound dimeric DNICs (Roussin's red esters (RREs)) accompanied by protein-bound monomeric DNICs (4:1 molar ratio) were observed on the basis of EPR and UV−vis spectra upon nitrosylation of the [4Fe-4S]$^{2+}$ clusters of FNR, a *hmp* gene transcription regulator.[7] In addition, inactivation of mitochondrial aconitases by nitrosylation led to the formation of DNICs displaying the rhombic EPR spectrum with g = 2.037, 2.031, 2.012,[4b] and an axial EPR spectrum with g = 2.006, 1.97, assigned as a d^9 DNICs, was observed upon the subsequent reduction by excess sodium dithionite.[4b] Moreover, reduction of HiPIP-containing protein-bound DNIC and the protein-bound DNIC obtained from nitrosylation of [2Fe-2S]$^+$ in the SoxR also revealed the same EPR spectrum proposed as d^9-DNIC.[4c,f]

In chemistry, the EPR-silent RREs-Cys were characterized when the aqueous solution of ferrous ion and thiol in a 1:2 molar ratio was nitrosylated by S-nitrosothiol, compared to the nitrosylation of the aqueous solution of ferrous ion and thiol (1:20 molar ratio) resulting in the production of the EPR-active DNICs-Cys.[8] Compared to the addition of excess of thiol into RREs-Cys solution leading to the transformation of RREs-Cys into DNICs-Cys, addition of sodium dithionite into RREs-Cys resulted in the formation of the proposed d^9-DNIC with EPR $g_\perp$= 2.01, $g_{||}$= 1.97 at 77 K.[8] According to the Enemark and Feltham notation,[9] the electronic structure/state of the M(NO)$_2$ unit of DNICs is generally designated as {M(NO)$_2$}^{n} (M = transition metal). We have shown that addition of H$^+$/SR$^-$ to DNICs/RREs, respectively, triggered the interconversion of DNICs and RREs.[6,10] Also, thiolate groups coordinated to the {Fe(NO)$_2$} motif play the key role in modulating the NO-releasing ability and stability of DNICs by tuning the electronic structure of DNICs.[6d] We also noticed that reduction of RREs to yield the proposed [Fe(μ-SR)(NO)$_2$]$_2^-$ (R = Me, Et) with EPR g = 1.995 at 250 K and [Fe(μ-SR)(NO)$_2$]$_2^{2-}$ characterized by IR and ^{1}H NMR spectra were reported, respectively, by Glidewell,[11] and Wojcicki.[12] In the recent communication, we reported that complexes [(^{t}BuS)$_2$Fe(NO)$_2$]$^-$ and [Fe(μ-S^{t}Bu)(NO)$_2$]$_2$ are in dynamic equilibrium in protic solvent MeOH. The subsequent addition of the equivalent of cobaltocene into the mixture MeOH solution of complexes [(^{t}BuS)$_2$Fe(NO)$_2$]$^-$ and [Fe(μ-S^{t}Bu)(NO)$_2$]$_2$ led to the formation of the fully delocalized [Fe(μ-S^{t}Bu)(NO)$_2$]$_2^-$ characterized by IR, UV−vis, EPR, SQUID, and single crystal X-ray diffraction.[13] In this manuscript, the steric effect of the nucleophiles ([EtS]$^-$ vs [^{t}BuS]$^-$ and [(EtS)$_2$Fe(NO)$_2$]$^-$ vs [(^{t}BuS)$_2$Fe(NO)$_2$]$^-$) on controlling the reduction and bridged-thiolate cleavage of RREs to yield the anionic Roussin's red esters [Fe(μ-SR)(NO)$_2$]$_2^-$ and DNICs [(RS)$_2$Fe(NO)$_2$]$^-$, respectively, was elucidated. Anionic Roussin's red esters *syn/anti*-[Fe(μ-SEt)(NO)$_2$]$_2^-$ were isolated and characterized by single-crystal X-ray diffraction, EPR, IR, and UV−vis spectra, and the equilibrium among [(EtS)$_2$Fe(NO)$_2$]$^-$, [Fe(μ-SEt)(NO)$_2$]$_2$, and [Fe(μ-SEt)(NO)$_2$]$_2^-$ in protic solvent MeOH was also studied.

Results and Discussion

Synthesis of the Anionic Roussin's Red Ester [cation]-[Fe(μ-SEt)(NO)$_2$]$_2$ (2a) (cation = Na$^+$-18-crown-6-ether (2a-Na), PPN$^+$ (2a-PPN), Me$_4$N$^+$ (2a-Me$_4$N)). After the THF solution of complex [Fe(μ-SEt)(NO)$_2$]$_2$ (**1a**),[14] [Na][biphenyl] (or KC$_8$) and 18-crown-6-ether (or [PPN][Cl]/[Me$_4$N][Cl]) was stirred at ambient temperature for 20 min (Scheme 1 a), reduction occurred to yield complex [cation][Fe(μ-SEt)(NO)$_2$]$_2$ (**2a**) (cation = PPN$^+$ (**2a-PPN**), Na$^+$-18-crown-6-ether (**2a-Na**), Me$_4$N$^+$ (**2a-Me$_4$N**)) identified by IR, UV−vis, EPR, magnetic susceptibility, and single-crystal X-ray diffraction. Complex **2a-PPN** exhibits diagnostic IR ν_{NO} stretching frequencies at 1673 s, 1655 s cm^{-1} (THF). The IR spectra for complexes **1a** and **2a-PPN** display the different pattern and position (1809 vw, 1774 s, 1749 s cm^{-1} for **1a** vs 1673 s, 1655 s cm^{-1} for **2a-PPN**). In comparison, the complex **1a** is dominated by three intense absorption

(3) (a) Salerno, J. C.; Ohnishi, T.; Lim, J.; King, T. E. *Biochem. Biophys. Res. Commun.* **1976**, *73*, 833–840. (b) Meyer, J. *Arch. Biochem. Biophys.* **1981**, *210*, 246–256.
(4) (a) Welter, R.; Yu, L.; Yu, C.-A. *Arch. Biochem. Biophys.* **1996**, *331*, 9–14. (b) Kennedy, M. C.; Anthonline, E. W.; Beinert, H. *J. Biol. Chem.* **1997**, *272*, 20340–20347. (c) Foster, M. W.; Cowan, J. A. *J. Am. Chem. Soc.* **1999**, *121*, 4093–4100. (d) Rogers, P. A.; Eide, L.; Klungland, A.; Ding, H. *DNA Repair 2* **2003**, 809–817. (e) Sellers, V. M.; Johnson, M. K.; Dailey, H. A. *Biochemistry* **1996**, *35*, 2699–2704. (f) Ding, H.; Demple, B. *Proc. Natl. Acad. Sci. U.S.A.* **2000**, *97*, 5146–5150.
(5) Cesareo, E.; Parker, L. J.; Pedersen, J. Z.; Nuccetelli, M.; Mazzetti, A. P.; Pastore, A.; Federici, G.; Caccuri, A. M.; Ricci, G.; Adams, J. J.; Parker, M. W.; Bello, M. L. *J. Biol. Chem.* **2005**, *280*, 42172–42180.
(6) (a) Tsai, M.-L.; Hsieh, C.-H.; Liaw, W.-F. *Inorg. Chem.* **2007**, *46*, 5110–5117. (b) Lu, T.-T.; Chiou, S.-J.; Chen, C.-Y.; Liaw, W.-F. *Inorg. Chem.* **2006**, *45*, 8799–8806. (c) Tsai, M.-L.; Liaw, W.-F. *Inorg. Chem.* **2006**, *45*, 6583–6585. (d) Tsai, F.-T.; Chiou, S.-J.; Tsai, M.-C.; Tsai, M.-L.; Huang, H.-W.; Chiang, M.-H.; Liaw, W.-F. *Inorg. Chem.* **2005**, *44*, 5872–5881. (e) Tsai, M.-L.; Chen, C.-C.; Hsu, I.-J.; Ke, S.-C.; Hsieh, C.-H.; Chiang, K.-A.; Lee, G.-H.; Wang, Y.; Chen, J.-M.; Lee, J.-F.; Liaw, W.-F. *Inorg. Chem.* **2004**, *43*, 5159–5167. (f) Hung, M.-C.; Tsai, M.-C.; Lee, G.-H.; Liaw, W.-F. *Inorg. Chem.* **2006**, *45*, 6041–6047.
(7) Cruz-Ramos, H.; Crack, J.; Wu, G.; Hughes, N. M.; Scott, C.; Thomson, J. A.; Green, J.; Poole, K. R. *EMBO J.* **2002**, *21*, 3235–3244.
(8) (a) Vanin, A. F. *Biochemistry (Moscow)* **1995**, *60*, 225–230. (b) Vanin, A. F.; Stukan, R. A.; Manukhina, E. B. *Biochim. Biophys. Acta* **1996**, *1295*, 5–12. (c) Costanzo, S.; Ménage, S.; Purrello, R.; Bonomo, R. P.; Fontecave, M. *Inorg. Chim. Acta* **2001**, *318*, 1–7.
(9) Enemark, J. H.; Feltham, R. D. *Coord. Chem. Rev.* **1974**, *13*, 339–406.
(10) (a) Chiang, C.-Y.; Miller, M. L.; Reibenspies, J. H.; Darensbourg, M. Y. *J. Am. Chem. Soc.* **2004**, *126*, 10867–10874. (b) Baltusis, L. M.; Karlin, K. D.; Rabinowitz, H. N.; Dewan, J. C.; Lippard, S. J. *Inorg. Chem.* **1980**, *19*, 2627–2632. (c) Reginato, N.; McCrory, C. T. C.; Pervitsky, D.; Li, L. *J. Am. Chem. Soc.* **1999**, *121*, 10217–10218.
(11) (a) Crayston, A. J.; Glidewell, C.; Lambert, J. R. *Polyhedron* **1990**, *9*, 1741–1746. (b) Glidewell, C. *Polyhedron* **1992**, *11*, 2803–2804.
(12) (a) Chau, C.-N.; Wojcicki, A. *Polyhedron* **1992**, *11*, 851–852. (b) Chau, C.-N.; Wojcicki, A. *Polyhedron* **1993**, *12*, 1261–1263.
(13) Tsou, C.-C.; Lu, T.-T.; Liaw, W.-F. *J. Am. Chem. Soc.* **2007**, *129*, 12626–12627.
(14) Thomas, J. T.; Robertson, J. H.; Cox, E. G. *Acta Crystallogr.* **1958**, *11*, 599–604.

Scheme 1

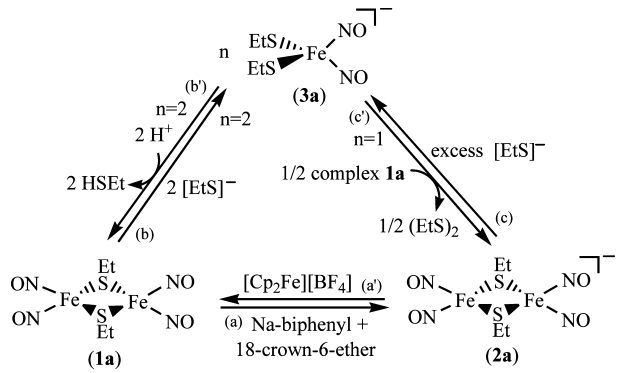

bands at 313, 363, 427(sh) nm (THF) in UV−vis spectrum, the electronic absorption spectrum of complex **2a-PPN** displays absorptions at 323, 370(sh), 452, 649, 970, 1030(sh) nm (THF) with an intense absorption 970 nm (extinction coefficient > 2000 L mol^{-1} cm^{-1}, Figure 1). Complex **2a-PPN** exhibits an axial EPR signal at $g_{\perp}$= 2.008, $g_{||}$= 1.968 at 77 K and an isotropic EPR signal at g = 1.997 at 298 K (Figure 2 a,b), deviated from the characteristic EPR signal (g = 2.03) of DNICs. The effective magnetic moment (μ_{eff}) decreases from 1.77 μ_B at 300 K to 1.72 μ_B at 4 K (Figure 3). In contrast to the Roussin's red esters with a $\{Fe(NO)_2\}^9$-$\{Fe(NO)_2\}^9$ coupling rationalizing the absence of paramagnetism and the EPR signal, the anionic Roussin's red ester **2a** is best described as a fully delocalized [$\{Fe(NO)_2\}^9$-$\{Fe(NO)_2\}^{10}$] complex, and the valence-trapped case can be unambiguously excluded from this result.

Structures. As shown in Table 1, the apparently longer Fe(1)···Fe(1A) distance (2.8413(6) Å) of complex **2a-PPN**, compared to that of 2.7080(5) Å in complex **1a** (Supporting Information, Figure S1),[14] indicates the weaker Fe(1)···Fe(1A) interaction in complex **2a-PPN**. Presumably, the electronic perturbation caused by the reduction of complex **1a** reduces the Fe(1)···Fe(1A) interaction to relieve the richness of electron density surrounding [$\{Fe(NO)_2\}^9$-$\{Fe(NO)_2\}^{10}$] [Fe(μ-$S)_2$Fe] centers.

Single-crystal X-ray structure of [Fe(μ-SEt)$(NO)_2]_2^-$ unit in $[PPN]^+$ salt is depicted in Figure 4 and selected bond dimensions are presented in the figure caption. The molecule is symmetrical because of a crystallographically imposed inversion center. Two nitrosyl groups and bridging thiolates

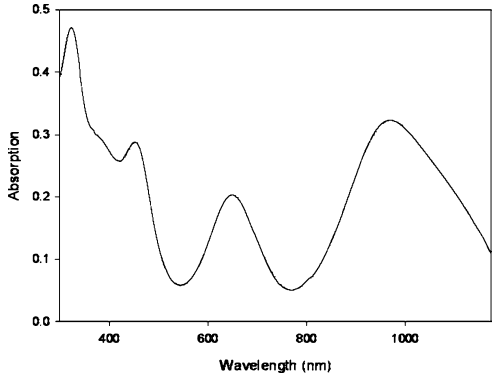

Figure 1. UV−vis spectrum of complex **2a-PPN** in THF at room temperature with absorption bands at 323, 370(sh), 452, 649, 970, and 1030(sh) nm.

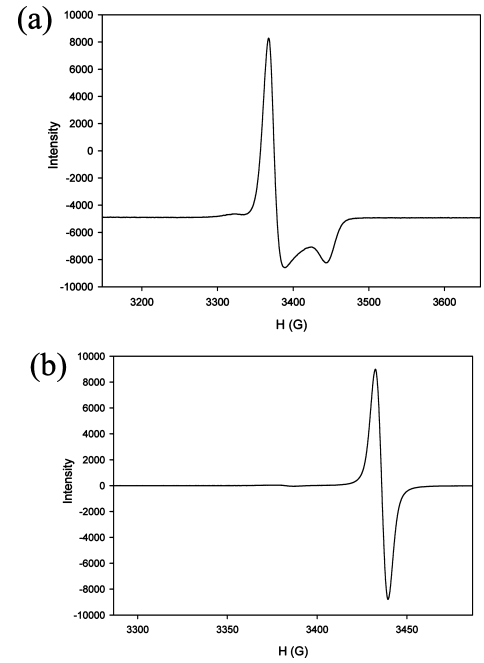

Figure 2. EPR spectrum of complex **2a-PPN** (THF) (a) $g_{\perp}$= 2.008, $g_{||}$= 1.968 at 77 K obtained with microwave power of 19.971 mW, frequency at 9.485 GHz, and modulation amplitude of 0.8 G at 100 KHz, and (b) g_{av} = 1.997 at 298 K obtained with a microwave power of 20.020 mW, frequency at 9.604 GHz, and modulation amplitude of 0.8 G at 100 KHz.

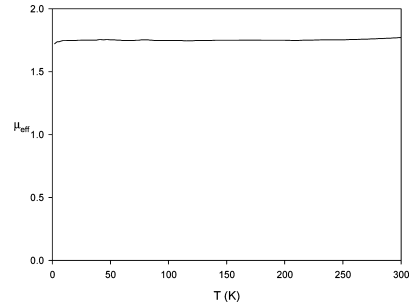

Figure 3. Plot of effective magnetic moment vs temperature (2−300 K) for complex **2a-PPN** under 0.5 T external magnetic field.

define the distorted tetrahedral geometry of each iron atom, leading to an acute angle Fe(1)−S(1)−Fe(1A) 76.43(2)° and S(1)−Fe(1)−S(1A) 103.57(2)°. The [Fe(μ-$S)_2$Fe] core geometry of complex **2a-PPN** is best described as a planar rhombus with two ethyl groups adopting *anti* configuration in the solid state (Figure 4). Compared to the bridging Fe(1)−S(1) and Fe(1)−S(1A) bond distances of 2.2608(5) and 2.2562(4) Å, respectively, found in complex **1a**,[14] the longer Fe(1)−S(1) and Fe(1)−S(1A) distances of 2.2968(6) and 2.2961(6) Å observed in complex **2a-PPN** indicate that reduction of complex **1a** yielding **2a-PPN** (reduction of [$\{Fe(NO)_2\}^9$-$\{Fe(NO)_2\}^9$] core to [$\{Fe(NO)_2\}^9$-$\{Fe(NO)_2\}^{10}$] core) results in the elongation of Fe(1)−S distances and the relief of Fe(1)···Fe(1A) interaction. Interestingly, the average Fe−N−O bond angle of 172.4(2)° in complex **2a-PPN** is distinct from that of 168.46(10)° in complex **1a**.[14] The most striking feature among complex **2a-PPN**, the neutral $\{Fe(NO)_2\}^{10}$ DNICs, and the $\{Fe(NO)_2\}^9$ DNICs is the differences of Fe−N(O)/N−O bond lengths. The mean N−O bond distance of 1.186(2) Å (1.181(2) and 1.190(2) Å) in

Table 1. Selected Metric Data for Neutral and Anionic Roussin's Red Esters

	2a-PPN	**2a-Na**	**2a-Me$_4$N**	**1a**[14]	[Fe(μ-S^{t}Bu)(NO)$_2$]$_2^-$[13]
Fe···Fe (Å)	2.8413(6)	2.8952(8)	2.8961(4)	2.7080(5)	2.9575(8)
Fe−S (Å)[a]	2.2965(6)	2.3032(8)	2.2968(6)	2.2585(5)	2.3031(8)
Fe−N (Å)[a]	1.661(2)	1.665(3)	1.661(2)	1.6747(11)	1.662(2)
N−O (Å)[a]	1.186(2)	1.187(3)	1.184(2)	1.1708(14)	1.186(3)
S···S (Å)	3.608	3.536	3.553	3.615	3.531
Fe−S−Fe ∠(deg)	76.43(2)	77.88(3)	78.17(2) [a]	73.671(14)	79.89(3)
S−Fe−S ∠(deg)	103.57(2)	102.12(3)	101.34(2)[a]	106.329(14)	100.11(3)
N−Fe−N ∠(deg)	120.96(9)	117.83(13)	118.72(10) [a]	116.10(5)	116.08(12)
Fe−N−O ∠(deg)[a]	172.44(19)	170.3(2)	170.5(2)	168.4(2)	169.5(2)
dihedral ∠(deg)[b]	180	180	168.3	180	180
torsion ∠(deg)	±2.61[c]	±0.76[c]	−2.12[d]/−0.37[e]	±1.83[c]	±2.02[c]

[a] Average bond distance and angle. [b] Defined by the intersection of the two Fe_2S zplanes. [c] $N_1-Fe_1-Fe_{1A}-N_{2A}$ and $N_2-Fe_1-Fe_{1A}-N_{1A}$ [d] $N_1-Fe_1-Fe_2-N_4$. [e] $N_2-Fe_1-Fe_2-N_3$.

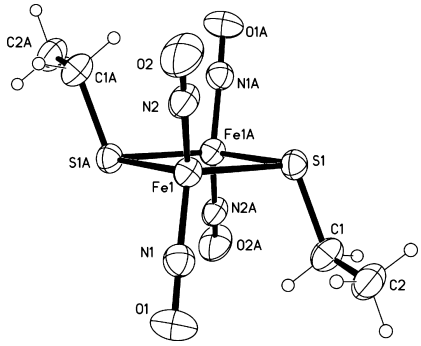

Figure 4. ORTEP drawing and labeling scheme of [Fe(μ-SEt)(NO)$_2$]$_2^-$ unit in [PPN]$^+$ salt with thermal ellipsoids drawn at 50% probability. Selected bond distances (Å) and angles (deg): Fe(1)···Fe(1A) 2.8413(6); Fe(1)−N(1) 1.6602(19); Fe(1)−N(2) 1.6619(18); Fe(1)−S(1) 2.2968(6); Fe(1)−S(1A) 2.2961(6); O(1)−N(1) 1.181(2); O(2)−N(2) 1.190(2); N(1)−Fe(1)−N(2) 120.96(9); N(1)−Fe(1)−S(1) 106.32(7); N(2)−Fe(1)−S(1) 107.31(7); N(1)−Fe(1)−S(1A) 105.38(7); N(2)−Fe(1)−S(1A) 111.86(7); S(1)−Fe(1)−S(1A) 103.57(2); O(1)−N(1)−Fe(1) 176.64(18); O(2)−N(2)−Fe(1) 168.23.

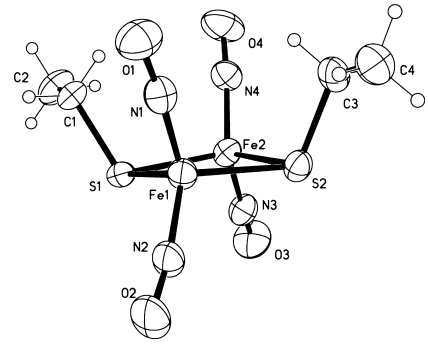

Figure 5. ORTEP drawing and labeling scheme of [Fe(μ-SEt)(NO)$_2$]$_2^-$ unit in [Me$_4$N]$^+$ salt with thermal ellipsoids drawn at 50% probability. Selected bond distances (Å) and angles (deg): Fe(1)···Fe(2) 2.8961(4); Fe(1)−N(1) 1.659(2); Fe(1)−N(2) 1.6624(19); Fe(2)−N(3) 1.6651(19); Fe(2)−N(4) 1.6585(19); Fe(1)−S(1) 2.2856(6); Fe(1)−S(2) 2.3091(6); Fe(2)−S(1) 2.2857(6); Fe(2)−S(2) 2.3067(6); O(1)−N(1) 1.180(2); O(2)−N(2) 1.185(2); O(3)−N(3) 1.188(2); O(4)−N(4) 1.183(2); N(1)−Fe(1)−N(2) 118.10(10); N(3)−Fe(2)−N(4) 119.34(10); N(1)−Fe(1)−S(1) 109.13(7); N(2)−Fe(1)−S(1) 106.69(7); N(1)−Fe(1)−S(2) 110.15(7); N(2)−Fe(1)−S(2) 110.08(7); N(3)−Fe(2)−S(1) 107.20(7); N(3)−Fe(2)−S(2) 110.06(7); N(4)−Fe(2)−S(1) 106.51(7); N(4)−Fe(2)−S(2) 110.70(7); S(1)−Fe(1)−S(2) 101.30(2); S(1)−Fe(2)−S(2) 101.37(2); O(1)−N(1)−Fe(1) 173.17(19); O(2)−N(2)−Fe(1) 168.1(2); O(3)−N(3)−Fe(2) 168.6(2); O(4)−N(4)−Fe(2) 171.98(19).

complex **2a-PPN**, longer than the average N−O bond distance of 1.171(1) Å observed in complex **1a**,[14] is nearly at the upper end of 1.178(3)−1.160(6) Å for the anionic {Fe(NO)$_2$}^{9} DNICs and nearly at the lower end of 1.214(6)−1.189(4) Å for the neutral {Fe(NO)$_2$}^{10} DNICs;[6f] meanwhile, the mean Fe−N(O) distance of 1.661(2) Å (1.660(2) and 1.662(2) Å) in complex **2a-PPN** also approaches the lower end of 1.695(3)−1.661(4) Å for the anionic {Fe(NO)$_2$}^{9} DNICs and the upper end of 1.650(7)−1.638(3) Å for the neutral {Fe(NO)$_2$}^{10} DNICs.[6f] In contrast to Roussin's red esters with a {Fe(NO)$_2$}^{9}-{Fe(NO)$_2$}^{9} coupling rationalizing the absence of paramagnetism and the EPR signal, the anionic Roussin's red ester **2a** is best described as a fully delocalized mixed-valence [{Fe(NO)$_2$}^{9}-{Fe(NO)$_2$}^{10}] complex. Obviously the EPR spectrum in combination with N−O and Fe−N(O) bond lengths may serve as an efficient tool for discrimination of the existence of {Fe(NO)$_2$}^{9} DNICs, {Fe(NO)$_2$}^{10} DNICs, the neutral Roussin's red esters and the anionic [{Fe(NO)$_2$}^{9}-{Fe(NO)$_2$}^{10}] Roussin's red esters.

The structure of the [Fe(μ-SEt)(NO)$_2$]$_2^-$ unit in [Me$_4$N]$^+$ salt is shown in Figure 5, and selected bond dimensions are presented in the figure caption. The [Fe(μ-S)$_2$Fe] core geometry of complex **2a-Me$_4$N** is best described as a butterfly like structure with two ethyl groups adopting a *syn* configuration and the dihedral angle of 168.3° (the intersection of the two Fe_2S planes) in the solid state. The structure of the [Fe(μ-SEt)(NO)$_2$]$_2^-$ unit in [Na$^+$-18-crown-6-ether] salt is shown in Supporting Information, Figure S2.

Interconversion among the Neutral Roussin's Red Ester 1a, the Anionic Roussin's Red Ester 2a, and Dinitrosyl Iron Complex [PPN][(EtS)$_2$Fe(NO)$_2$] (3a). Reversibly, the direct conversion of complex **2a** to complex **1a** was observed when THF solution of complex **2a** was treated with [Cp$_2$Fe][BF$_4$] at ambient temperature (Scheme 1a′). Obviously, this anionic dimeric dinitrosyl iron complex containing [{Fe(NO)$_2$}^{9}-{Fe(NO)$_2$}^{10}] core undergoes a reversible one-electron redox process. Compared to the quantitative transformation of complex **1a** to **3a** in the reaction of complex **1a** and 2 equiv of [EtS]$^-$ in CH_3CN (Scheme 1b), the excess (4-fold) of [EtS]$^-$ was needed to trigger 1 equiv of complex **2a** to transform into complex **3a** in CH_3CN at ambient temperature (Scheme 1c). Presumably, it is attributed to the electronic richness of the [{Fe(NO)$_2$}^{9}-{Fe(NO)$_2$}^{10}] core of complex **2a**. The reaction was monitored by IR ν_{NO} spectra; the shift of the stretching frequencies from 1675 s, 1658 s cm^{-1} to 1722 s, 1680 s cm^{-1} confirmed the formation of complex **3a** accompanied by the presumed extremely unstable [(EtS)$_2$Fe(NO)$_2$]$^{2-}$ (IR ν_{NO} 1625 m, 1580 sh cm^{-1} (CH_3CN)) ($E_{1/2}$ ([(EtS)$_2$Fe(NO)$_2$]$^-$/[(EtS)$_2$Fe-

$(NO)_2]^{2-}$) = −1.688 V in CH_3CN vs Fc^+/Fc, $E_a - E_c$ = 168 mV, Supporting Information, Figure S3). In contrast to the bridged-thiolate cleavage yielding the anionic $\{Fe(NO)_2\}^9$ complex **3a** by addition of 2 equiv of $[EtS]^-$ to complex **1a** (Scheme 1b), addition of complex **3a** to complex **1a** in a 2:1 molar ratio triggered reduction of complex **1a** to yield the anionic Roussin's red ester **2a** accompanied by byproduct $(EtS)_2$ identified by ^1H NMR (Scheme 1c′). Instead of reduction of complex **1a** yielding complex **2a**, the coexistence of complexes **3a** and **1a** was observed immediately when complex **1a** was reacted with 1 equiv of $[EtS]^-$ in CH_3CN at ambient temperature, and the reaction solution finally led to the formation of complex **2a** and byproduct $(EtS)_2$ because of the repeated cleavage of bridged-thiolates of complex **1a** yielding complex **3a** by $[EtS]^-$, followed by reduction of complex **1a** by complex **3a**. Presumably, the concurrent nucleophilic attack of $[EtS]^-$ on $\{Fe(NO)_2\}$ cores, respectively, triggers the bridged-thiolate cleavage of complex **1a** via the proposed intermediate **A** (shown below) to yield complex **3a** when the CH_3CN solution of complex **1a** was treated with 2 equiv of $[EtS]^-$, whereas anionic complex **3a** prefers the nucleophilic attack of the terminal ethylthiolate on the $\{Fe(NO)_2\}$ cores yielding complex **2a**, $(EtS)_2$ and a half equiv of complex **1a** via the proposed intermediate **B** (shown below). It is presumed that complex **3a** serves as the thiolates carrier to induce the nucleophilic attack of the coordinated thiolates on the $\{Fe(NO)_2\}$ cores to yield complex **2a** ($E_{1/2}^{0/1-}$ = −0.95 V (complex **1a**),[11a] E_a = −0.258 V ($\{Fe(NO)_2\}^9/\{Fe(NO)_2\}^8$ for complex **3a**, Supporting Information, Figure S4), E_a = −2.767 V ($[EtS]^-$) vs $FeCp_2/FeCp_2^+$). These results illustrate one aspect of how the nucleophiles ($[EtS]^-$ vs $[(EtS)_2Fe(NO)_2]^-$) function to control the reaction pathways (bridged-thiolate cleavage vs reduction) upon reaction of complex **1a** and nucleophiles.

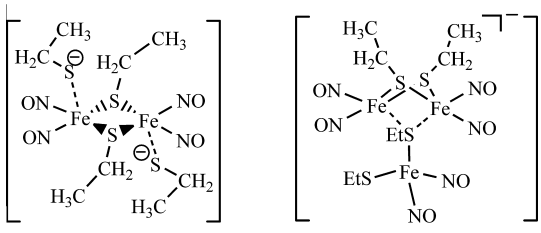

(A) (B)

Transformation of Complex 3a to Complex 2a. The complete conversion of complex **3a** to complex **2a** was observed when complex **3a** was dissolved in CH_3CN and stirred at 50 °C for 1 week. Presumably, the formation of complex **2a** was initiated by the thermodynamic instability of the CH_3CN solution of complex **3a**. The transformation of complex **3a** into complex **2a** in CH_3CN may be accounted for by the following sequences; the degradation of complex **3a** led to the buildup of the unstable, neutral intermediate $[(EtS)Fe(NO)_2]$ (**C**) species and the released $[EtS]^-$ (Scheme 2a). This highly reactive species **C** is driven to the formation of complex **1a** via dimerization. The subsequent reduction of complex **1a** by complex **3a** in combination with the successive formation of complex **3a** via the repeatedly

Scheme 2

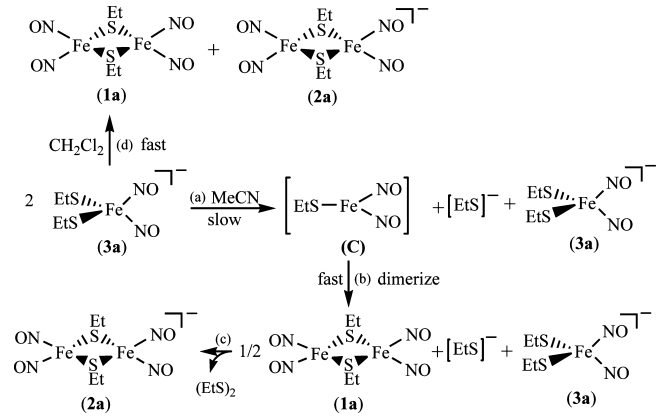

bridged-thiolate cleavage of complex **1a** by $[EtS]^-$ explains the formation of complex **2a** as the only product when complex **3a** was dissolved in CH_3CN (Scheme 2a−c). Because the nucleophilic attack of thiolates on CH_2Cl_2 to release chloride is well-known,[15] the transformation of complex **3a** dissolved in CH_2Cl_2 was also investigated. Instead of the formation of complex **2a** as the only product (except for $(EtS)_2$ and $[EtS]^-$) observed in the CH_3CN solution of complex **3a** (Scheme 2a−c), CH_2Cl_2 solution of complex **3a** rapidly converted into complex **1a** along with complex **2a** at ambient temperature (Scheme 2d). Because of the rapid nucleophilic displacement reaction between the released $[EtS]^-$ and CH_2Cl_2, the released ethyl thiolates from degradation of complex **3a** depleted to prevent the repeated formation of complex **3a** via the bridged-thiolate cleavage of complex **1a** by $[EtS]^-$ rationalizes the formation of complex **1a** and complex **2a** upon dissolution of complex **3a** in CH_2Cl_2 at ambient temperature (Scheme 2d).

In contrast to the dynamic equilibrium of $[(^tBuS)_2Fe(NO)_2]^-$ (**3b**) and $[Fe(\mu\text{-}S^tBu)(NO)_2]_2$ (**1b**) observed in dissolution of complex **3b** in MeOH,[13] dissolution of complex **3a** in MeOH led to the formation of a mixture of complex **2a** and trace of complex **3a** at 298 K for 17 days, characterized by EPR spectra (Figure 6). Presumably, the conversion of complex **3a** to complex **2a** in MeOH was driven initially by the formation of $[(MeOH)_n\cdots SEt]^-$ and complex **1a** (Scheme 3a), followed by the subsequent reduction of complex **1a** by complex **3a** to produce the stable

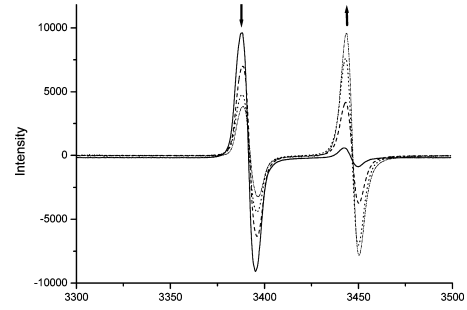

Figure 6. Conversion of complex **3a** (in MeOH) to complex **2a** monitored by EPR at 298 K. The isotropical signal at g = 2.029 (complex **3a**) decreases with increase of the isotropical signal at g = 1.997 (complex **2a**) at 298 K obtained with a microwave power of 5.016 mW, frequency at 9.633 GHz, and modulation amplitude of 0.8 G at 100 KHz. (time interval: solid, 1 h; dashed, 3 d; dotted, 7 d; dashed-dotted, 17 d).

Scheme 3

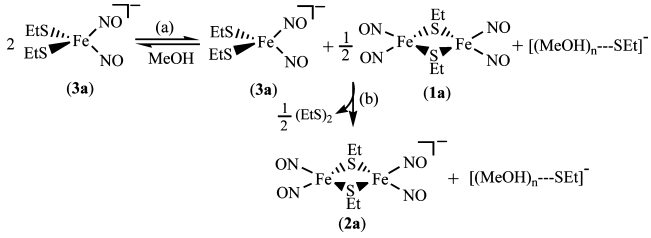

Scheme 4

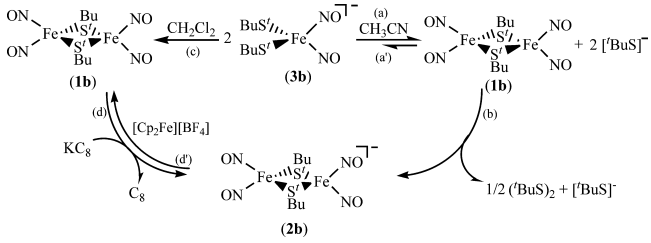

complex **2a** (Scheme 3b). The transformation of complex **3a** to complex **2a** was monitored by EPR at 298 K; the isotropic signal at $g = 2.029$ decreases accompanied by the simultaneous formation of another isotropic signal at $g = 1.997$ (formation of complex **2a**, Figure 6). This result further demonstrates that complex **3a** triggers reduction of complex **1a** to produce the anionic Roussin's red ester **2a**.

Transformation of {Fe(NO)$_2$}^{9} [Na-18-crown-6-ether][(^{t}BuS)$_2$Fe(NO)$_2$] (3b) into [Fe(μ-S^{t}Bu)(NO)$_2$]$_2$ (1b) and [Na-18-crown-6-ether][Fe(μ-S^{t}Bu)(NO)$_2$]$_2$ (2b). To further examine the effect of steric modulations of the monodentate coordinated ligand [RS]$^-$ on the stability and transformation reactivity of the anionic {Fe(NO)$_2$}^{9} [(RS)$_2$Fe(NO)$_2$]$^-$, complex [(^{t}BuS)$_2$Fe(NO)$_2$]$^-$ (**3b**) containing coordinated *tert*-butylthiolates was investigated.[13,16] Complex **3b** is extremely unstable, compared to the analogue **3a**, in CH_3CN at room temperature. As shown in Scheme 4a,b, complex **3b** converted into complex [Fe(μ-S^{t}Bu)(NO)$_2$]$_2^-$ (**2b**) when complex **3b** was dissolved in CH_3CN and stirred at room temperature for 4 days. Obviously, the alkylthiolates [^{t}BuS]$^-$ and [EtS]$^-$, rendering the {Fe(NO)$_2$}^{9} unit in different electronic/structural environments, induce different stability to the {Fe(NO)$_2$}^{9} fragment.

As observed in the transformation of complex **3a** into complex **2a** in CH_3CN, it is presumed that dissociation of the coordinated [^{t}BuS]$^-$ ligand of the unstable complex **3b** resulted in the buildup of the unstable intermediate [(^{t}BuS)-Fe(NO)$_2$], which subsequently dimerized to yield complex [Fe(μ-S^{t}Bu)(NO)$_2$]$_2$ (**1b**) and the released [^{t}BuS]$^-$ (Scheme 4a). In contrast to the complete bridged-thiolate cleavage of complex **1a** yielding complex **3a** observed in the reaction of 2 equiv of [EtS]$^-$ and complex **1a** (Scheme 1b), the simultaneous reduction and bridged-thiolate cleavage of complex **1b** by [^{t}BuS]$^-$ yielding complex **2b** and complex **3b** were observed spectrally (Scheme 4b,a'), and this reaction finally led to the complete reduction of complex **1b** yielding the thermodynamically stable complex **2b** after the mixture solution was stirred at ambient temperature for 96 h. Presumably, the nucleophilic attack of one bulky *tert*-butylthiolate ligand on both {Fe(NO)$_2$} cores leading to the formation of complex **2b** via intermediate **D** (shown below), and the concurrent nucleophilic attack of [^{t}BuS]$^-$ on each {Fe(NO)$_2$} core leading to the formation of complex **3b** via intermediate **E** (shown below) may occur simultaneously. Obviously, the steric effect of nucleophiles ([EtS]$^-$ vs [^{t}BuS]$^-$) plays the critical role in modulating the binding modes between the Roussin's red esters and nucleophiles and subsequently leading to the different products.

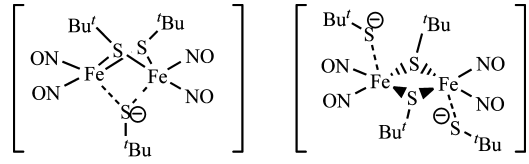

To further corroborate the interacting modes between nucleophiles and neutral Roussin's red esters controlling the reaction types (bridged-thiolate cleavage vs reduction), the transformation of complex **3b** in CH_2Cl_2 was also investigated. In contrast to the conversion of complex **3a** to complexes **1a** and **2a** observed in CH_2Cl_2 solution of complex **3a** at room temperature for 2 h, the direct transformation of complex **3b** into complex **1b** in CH_2Cl_2 was observed at ambient temperature for 20 min. During this transformation, no product **2b** was detected spectrally because of the rapid dechlorination reaction between the released [^{t}BuS]$^-$ and CH_2Cl_2 (Scheme 4c) and the inertness of complex **3b** toward complex **1b**. Thus, the steric structure of DNICs appears crucial for initiating the nucleophilic attack of DNICs on Roussin's red esters and triggering reduction of Roussin's red esters. That is, transformation of the anionic DNICs [(RS)$_2$Fe(NO)$_2$]$^-$ into either the anionic Roussin's red esters or the neutral Roussin's red esters (or both) may be tailored by the coordinated ligands [RS]$^-$ of DNICs and solvents (surroundings).

X-ray Absorption Spectroscopy. To clarify the detailed electronic structure (oxidation state) of the iron in complex **2a**, the X-ray absorption measurements were undertaken. The K-edge absorption spectra of complexes **1a** and **2a-PPN** are displayed in Figure 7. A typical Fe(0) of Fe foil, Fe(II) of FeO and a tetrahedral Fe(I) of [(S−S$_3$-S)Fe(NO)$_2$]$^-$ are included for references.[6e,17] As shown in Figure 7a, the absorption edge E_0 of Fe(I) complex **1a** is higher than that of Fe(0) but lower than that of Fe(II) of FeO. The absorption spectra of both complex **1a** and complex **2a-PPN** are displayed in Figure 7b, where the symmetry allowed pre-edge 1s→3d transitions are enlarged in the inset with 7113.8

(15) (a) Lee, C.-M.; Chuang, Y.-L.; Chiang, C.-Y.; Lee, G.-H.; Liaw, W.-F. *Inorg. Chem.* **2006**, *45*, 10895–10904. (b) Lucchese, B.; Humphreys, K. J.; Lee, D.-H.; Incarvito, C. D.; Sommer, R. D.; Rheingold, A. L.; Karlin, K. D. *Inorg. Chem.* **2004**, *43*, 5987–5998.

(16) Harrop, T. C.; Song, D.; Lippard, S. J. *J. Am. Chem. Soc.* **2006**, *128*, 3528–3529.

(17) Hsu, I.-J.; Hsieh, C.-H.; Ke, S.-C.; Chiang, K.-A.; Lee, J.-M.; Chen, J.-M.; Jang, L.-Y.; Lee, G.-H.; Wang, Y.; Liaw, W.-F. *J. Am. Chem. Soc.* **2007**, *129*, 1151–1159.

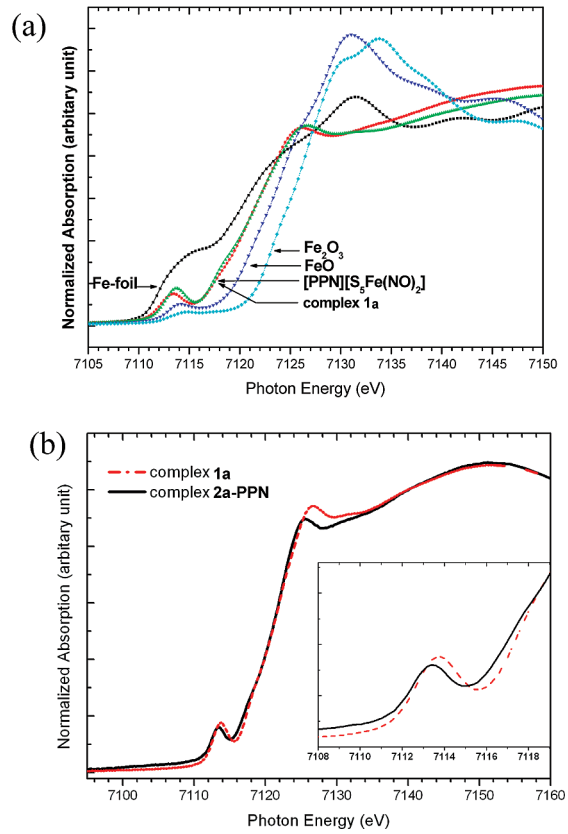

Figure 7. (a) Fe K-edge spectra of the complex **1a** and the reference compounds (Fe foil, FeO and $[PPN][S_5Fe(NO)_2]$). (b) Fe K-edge spectra of the complexes **1a** (dashed) and **2a-PPN** (solid).

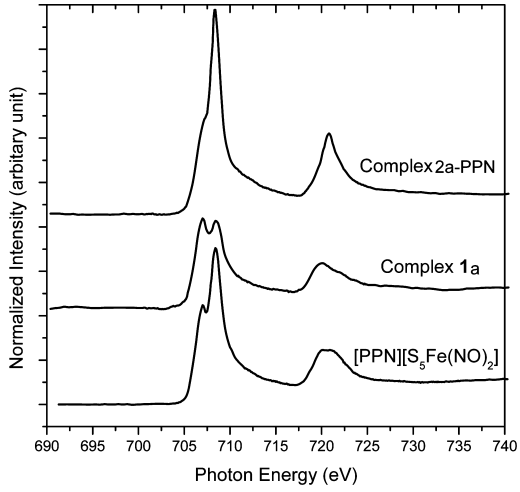

Figure 8. Fe L-edge spectra of the complexes **1a**, **2a-PPN**, and the reference compound ($[PPN][S_5Fe(NO)_2]$).

and 7113.4 eV for complex **1a** and **2a-PPN**, respectively. According to previous report by Solomon et al.,[18] the lower pre-edge transition peak of **2a-PPN** than that of complex **1a** may indicate the lower oxidation state of Fe in complex **2a-PPN**. The Fe $L_{III,II}$-edge absorption spectrum of complex **2a-PPN** is depicted in Figure 8 together with those of complexes **1a** and $[S_5Fe(NO)_2]^-$. The main L_{III} peak at 708.4 eV was observed with a shoulder at 707.0 eV for both complexes **2a-PPN** and $[S_5Fe(NO)_2]^-$,[6e] but with a peak at

(18) Westre, T. E.; Kennepohl, P.; DeWitt, J. G.; Hedman, B.; Hodgson, K. O.; Solomon, E. I. *J. Am. Chem. Soc.* **1997**, *119*, 6297–6314.

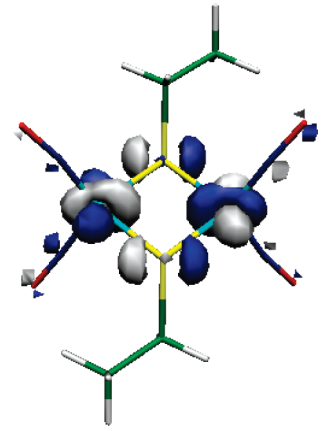

Figure 9. SOMO of complex **2a-PPN.**

707.0 eV for complex **1a**. This indicates that all three complexes have similar oxidation states. As complex **2a-PPN** is a one electron reduction from complex **1a** and the local geometry of both Fe sites are the same, the significant differences in intensities between complex **2a-PPN** and **1a** at L_{III} indicate that one electron reduction mainly affects the number of unoccupied d-orbital states. According to the Fe K- and $L_{III,II}$-edge absorption spectra, the reduction from complex **1a** to **2a-PPN** is mainly happening at the Fe sites.

MO Calculation. Unrestricted open shell MO calculations have been applied to the complex **2a** anion. The unrestricted one yields the expectation value of total spin quantum number,[19] $\langle S^2 \rangle$, of 0.80, which is close to the ideal eigenvalue of 0.75 with $S = 1/2$. The atomic charge analysis yields roughly the same charge on each iron atom of anion **2a**, regardless which type of atomic partition is taken into account. The calculated isotropic g-value is 1.998 at ground-state in good agreement with the one derived from room temperature EPR. The singly occupied molecular orbital (SOMO) of complex **2a** is depicted in Figure 9, where the major contribution is obviously from both Fe atoms and its bonded S ligands with ~50% $d_{x^2-y^2}$ and its associated S ligands with ~ 25% p_x orbitals. Thus, the unpaired electron of anion **2a** is delocalized in the plane with main contribution from two Fe atoms with spin density of ~0.65 e in each Fe site. Moreover, the antibonding character between the two Fe ions of the SOMO explains well that the Fe···Fe distance of anion **2a** is longer than that of **1a**. This result is consistent with the crystallographic data listed in Table 1 in comparison with complex **1a**. To realize if any uneven distribution of the unpaired electron could exist between two Fe sites, a broken symmetry state with C_1 symmetry geometry was tried; the results, however, show the same as those from the symmetric ones.

The time-dependent density functional theory (TDDFT) calculation results indicate that the first absorption peak is mainly derived from a SOMO with A_u symmetry to a lowest unoccupied molecular orbital (LUMO) with A_g symmetry at the 1050 nm. The LUMO is displayed in Figure 10, and

(19) (a) Bulo, R. E.; Ehlers, A. W.; Grimme, S.; Lammertsma, K. *J. Am. Chem. Soc.* **2002**, *124*, 13903–13910. (b) Szabo, A.; Ostlund, N. S. *Modern Quantum Chemistry*, 1st ed. Revised; McGraw-Hill: New York, 1989; p 107.

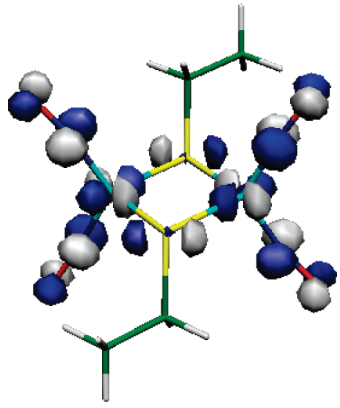

Figure 10. LUMO of complex **2a-PPN.**

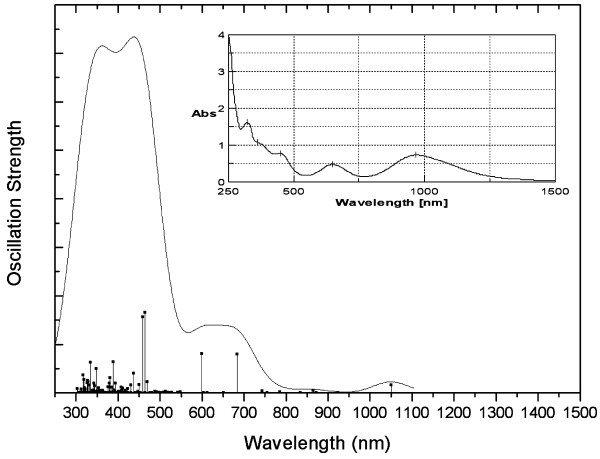

Figure 11. Simulated and experimental UV−vis spectra of complex **2a-PPN**.

it reveals that the orbital is predominately contributed from the NO, Fe, and S with 57%, 26%, and 16%, respectively. Therefore, the broad absorption peak around 970 (1050 sh) nm may be attributed to the Fe → NO(π^*) together with contribution from intervalence transition of two irons in the fully delocalized complex **2a-PPN**, and all the other transitions are related to the charge transfer between metal and S or NO ligands. All TDDFT calculation results are depicted in Figure 11.

Conclusion and Comments

Studies on the interconversion among DNICs [(RS)$_2$Fe(NO)$_2$]$^-$, dimeric DNICs [Fe(μ-SR)(NO)$_2$]$_2$, and anionic dimeric DNICs [Fe(μ-SR)(NO)$_2$]$_2^-$ (R = Et, ^{t}Bu) have led to the following results, including certain results from earlier studies.[13]

(1) The steric effect of nucleophiles ([EtS]$^-$ vs [^{t}BuS]$^-$) plays the critical role in determining the reaction product upon Roussin's red esters reacted with nucleophiles [RS]$^-$ (i.e., the complete bridged-thiolate cleavage yielding DNIC **3a** in the reaction of [EtS]$^-$ and complex **1a** vs the bridged-thiolate cleavage in combination with reduction producing complex **3b** and the anionic Roussin's red ester **2b** in the reaction of [^{t}BuS]$^-$ and complex **1b**). Presumably, the nucleophilic attack of one bulky thiolate (e.g., [^{t}BuS]$^-$) on both {Fe(NO)$_2$} cores of Roussin's red ester leads to the reduction of Roussin's red ester. In contrast, the nucleophilic attack of the less bulky thiolates (e.g., [EtS]$^-$) on each {Fe(NO)$_2$} core of Roussin's red ester triggers the bridged-thiolate cleavage to produce DNICs.

(2) In contrast to the complete inertness of DNIC **3b** toward complex **1b**, nucleophile DNIC **3a** induces reduction of complex **1a** to produce the anionic Roussin's red ester **2a**. This result rationalizes that dissolution of complex **3a** in MeOH at 298 K finally led to the formation of a mixture of complexes **2a** and **3a**, in contrast to the dynamic equilibrium of complexes **3b** and **1b** observed in dissolution of complex **3b** in MeOH.[13] Conclusively, these results illustrate the aspect of how the steric effect of nucleophiles ([(EtS)$_2$Fe(NO)$_2$]$^-$ vs [(^{t}BuS)$_2$Fe(NO)$_2$]$^-$) functions to determine the reaction pathways (reduction vs no reaction) and the products.

(3) On the basis of MO calculation, X-ray absorption (Fe K- and L-edge), EPR, and SQUID, the electronic structure of the fully delocalized [{Fe(NO)$_2$}^{9}-{Fe(NO)$_2$}^{10}] complex **2a** is best described as the dynamic resonance hybrid of [{Fe$^+$(•NO)$_2$}^{9}-{Fe^0(•NO)$_2$}^{10}] and [{Fe^0(•NO)$_2$}^{10}-{Fe$^+$-(•NO)$_2$}^{9}]. The unpaired electron of the anion **2a** is evenly distributed between the two Fe sites according to the result of the MO calculation; this may provide an explanation for the mixed-valence property of complex **2a**.

(4) The electronic configuration of [Fe(μ-S)$_2$Fe] core is rearranged in going from [{Fe(NO)$_2$}^{9}-{Fe(NO)$_2$}^{9}] complex **1a/1b** to the fully delocalized [{Fe(NO)$_2$}^{9}-{Fe(NO)$_2$}^{10}] complexes **2a/2b** which minimizes the degree of the Fe···Fe interaction to stabilize complexes **2a/2b**.[16,17]

(5) In inorganic chemistry, the EPR spectrum in combination with the N—O and Fe—N(O) bond lengths may serve as an efficient tool for the discrimination of the existence of the anionic {Fe(NO)$_2$}^{9} DNICs, the neutral {Fe(NO)$_2$}^{10} DNICs, the neutral Roussin's red ester, and the anionic fully delocalized [{Fe(NO)$_2$}^{9}-{Fe(NO)$_2$}^{10}] RREs.

(6) The spontaneous transformation of the anionic {Fe(NO)$_2$}^{9} DNICs into RREs or anionic RREs occurs in the aprotic/protic solvents.

It has been reported that nitrosylation of murine L1210 leukemia cells, promoted by the adjacent BCG-/IRN-γ-activated macrophages in vivo, led to the formation of DNICs accompanied by the uncharacterized axial EPR signal g ∼ 2,[20a] identical to the g value of the anionic RREs.[13] In the activated macrophages from mice infected with *Mycobacterium bovis*, although enhancing the amount of nitric oxide from L-arginine rationalizes the increasing intensity of the peak g ∼ 2.03,[20b] it is presumed that the extra-added L-cysteine may lead to the direct reduction of protein-bound RREs or produce the mobile LMW-DNICs to trigger the production of the anionic RREs.[20b,c] The results of this study may decipher/predict that the protein-bound DNICs do not trigger the reduction of protein-bound RREs because of steric hindrance or immobilization, whereas one cannot rule out the possibility of reduction of protein-bound RREs induced by pendant cysteinate of proteins in the biological system.

This study also implies that nitrosylation of [Fe−S] clusters may produce DNICs accompanied by the corre-

sponding Roussin's red esters and anionic Roussin's red esters resulting from the transformation of DNICs in biological system,[4b,c] since conversion of DNICs into neutral/anionic dimeric DNICs occurs in solvents.[13] The EPR-silent dimeric DNICs may be ignored in the nitrosylation of [Fe−S] clusters. Therefore, the EPR spectrum in combination with IR and UV−vis spectra may be employed to serve as an efficient tool to examine the degradation of [Fe−S] clusters via nitrosylation. On the other hand, although these anionic Roussin's red ester forms have no known role yet in the H_2-production chemistry, they are useful analogs of related [Fe]-only hydrogenases where mixed-valence forms ($[Fe^{I}Fe^{0}]$) are suggested to be involved in the biological functions.[21]

Experimental Section

Manipulations, reactions, and transfers were conducted under nitrogen according to Schlenk techniques or in a glovebox (N_2 gas). Solvents were distilled under nitrogen from appropriate drying agents (diethyl ether from CaH_2; acetonitrile from $CaH_2-P_2O_5$; methylene chloride from CaH_2; methanol from Mg/I_2; hexane and tetrahydrofuran (THF) from sodium benzophenone) and stored in dried, N_2-filled flasks over 4 Å molecular sieves. Nitrogen was purged through these solvents before use. Solvent was transferred to the reaction vessel via stainless cannula under positive pressure of N_2. Complexes $[Fe(\mu\text{-SEt})(NO)_2]_2$, $[(EtS)_2Fe(NO)_2]^-$, and $[(^tBuS)_2Fe(NO)_2]^-$ were synthesized based on the literature methods.[6b,13,14] The reagents ethylthiol (Aldrich), 2-methyl-2-propanthiol (Aldrich), sodium (Nihon Seiyaku Industries), biphenyl (Lancaster), 18-crown-6-ether (TCI), bis(triphenylphosphoranylidene) ammonium chloride ([PPN][Cl], Fluka), tetramethylammonium chloride ([Me_4N][Cl], TCI) and ferrocenium tetrafluoroborate ([Cp_2Fe][BF_4], Aldrich) were used as received. Infrared spectra of the ν_{NO} stretching frequencies were recorded on a PerkinElmer model spectrum One B spectrometer with sealed solution cells (0.1 mm, CaF_2 windows). UV−vis spectra were recorded on a Jasco V-570 spectrometer. Electrochemical measurements were performed with CHI model 421 potentiostat (CH Instrument) instrumentation. Cyclic voltammograms were obtained from 10 mM analyte concentration in O_2-free CH_3CN using 0.2 M [n-Bu_4N][PF_6] as a supporting electrolyte. Potential was measured at 298 K vs a Ag/AgCl reference electrode by using a glassy carbon working electrode. Analyses of carbon, hydrogen, and nitrogen were obtained with a CHN analyzer (Heraeus).

Preparation of [cation][Fe(μ-SEt)$(NO)_2]_2$ (2a) (cation = Na-18-crown-6-ether (2a-Na), PPN^+ (2a-PPN), Me_4N^+ (2a-Me_4N)). Method A. Compounds biphenyl (0.019 g, 0.12 mmol) and excess sodium metal (0.023 g, 1 mmol) were dissolved in THF (10 mL) and stirred under N_2. Upon the color of the sodium-biphenyl solution changing into deep purple, the sodium-biphenyl solution was added slowly to the THF solution (5 mL) of complex **1a** (0.035 g, 0.1 mmol) and 18-crown-6-ether (0.026 g, 0.1 mmol) via cannula under positive N_2. The reaction was monitored with FTIR, and the IR ν_{NO} shifting from 1809 vw, 1774 s, 1749 s cm^{-1} to 1673 s, 1655 s cm^{-1} were observed. After being stirred for 10 min, diethyl ether (15 mL) was added to the deep green solution. The deep green solution was filtered through Celite to remove the insoluble solid, and then hexane was added into the filtrate to precipitate the dark-green [Na-18-crown-6-ether][Fe(μ-SEt)$(NO)_2]_2$ (**2a-Na**, yield 0.056 g, 87%). Recrystallization from THF solution of complex **2a-Na** layered with hexane at −20 °C for a week led to the dark-green crystals suitable for X-ray crystallography. IR ν_{NO}: 1673 s, 1655 s cm^{-1} (THF); 1675 s, 1658 s cm^{-1} (CH_3CN); 1672 s, 1653 s cm^{-1} (CH_2Cl_2). Absorption spectrum (THF) [nm, $\lambda_{max}(M^{-1}\ cm^{-1}, \varepsilon)$]: 319 (5500), 370 sh (3600), 453 (3300), 649 (2300), 970 (3500), 1030 sh. Method B. Complexes [PPN][$(EtS)_2Fe(NO)_2$] (**3a**, 0.155 g, 0.2 mmol) and [Fe(μ-SEt)$(NO)_2]_2$ (**1a**, 0.035 g, 0.1 mmol) were dissolved in THF (10 mL) and stirred overnight under nitrogen at ambient temperature. The reaction was monitored with FTIR, and the IR ν_{NO} shifting from 1809 vw, 1774 s, 1749 s, 1715 s, 1673 s cm^{-1} to 1673 s, 1655 s cm^{-1} were observed. Diethyl ether (10 mL) was added to the dark-green solution. The dark-green solution was filtered through Celite, and then hexane was added into the filtrate to separate the dark-green precipitate [PPN][Fe(μ-SEt)$(NO)_2]_2$ (**2a-PPN**, yield 0.140 g, 79%) and the solution which was dried and characterized by ^1H NMR as $(EtS)_2$. Recrystallization from THF solution of complex **2a-PPN** layered with hexane at −20 °C for a week led to the dark-green crystals suitable for X-ray crystallography. IR ν_{NO}: 1673 s, 1655 s cm^{-1} (THF); 1675 s, 1658 s cm^{-1} (CH_3CN); 1672 s, 1653 s cm^{-1} (CH_2Cl_2). Absorption spectrum (THF) [nm, $\lambda_{max}(M^{-1}\ cm^{-1}, \varepsilon)$]: 323 (5100), 370 sh (3300), 452 (3100), 649 (2200), 970 (3500), 1030 sh. Anal. Calcd for $C_{40}H_{40}N_5O_4P_2S_2Fe_2$: C, 53.83; H, 4.52; N, 7.85. Found: C, 53.91; H, 4.70; N, 7.95. Complex [Me_4N][Fe(μ-SEt)$(NO)_2]_2$ (**2a-Me_4N**, yield 0.071 g, 84%) was prepared in the same manner. Recrystallization from THF solution of complex **2a-Me_4N** layered with hexane at −20 °C for a week led to the dark-green crystals suitable for X-ray crystallography. IR ν_{NO}: 1673 s, 1655 s cm^{-1} (THF); 1675 s, 1658 s cm^{-1} (CH_3CN); 1672 s, 1653 s cm^{-1} (CH_2Cl_2). Absorption spectrum (THF) [nm, $\lambda_{max}(M^{-1}\ cm^{-1}, \varepsilon)$]: 321 (7400), 370sh (4700), 449 (3600), 649 (2300), 973 (3500), 1030sh.

Reaction of Complex 1a and 2 equiv of [PPN][SEt]. Complex **1a** (0.035 g, 0.1 mmol) and [PPN][SEt] (0.120 g, 0.2 mmol) were dissolved in CH_3CN (5 mL). The mixture reaction solution was stirred at ambient temperature for 10 min. IR ν_{NO} spectrum displaying two strong stretching bands at 1722 s, 1680 s cm^{-1} (CH_3CN) implicated the formation of complex **3a**. The yellow-brown solution was dried under vacuum and redissolved in THF-diethyl ether. The solution was then filtered through Celite, and hexane was added into the filtrate to precipitate the brown product complex **3a** (yield 0.119 g, 77%) characterized by FTIR and UV−vis.

Reaction of Complex 1a and 1 equiv of [PPN][SEt]. Complex **1a** (0.035 g, 0.1 mmol) and [PPN][SEt] (0.060 g, 0.1 mmol) were dissolved in CH_3CN (5 mL). The reaction solution was stirred under nitrogen at ambient temperature and monitored by FTIR immediately. The IR ν_{NO} spectrum of the reaction solution showing absorption bands at 1810 vw, 1776 s, 1750 s, 1722 s, 1680 s cm^{-1} implicated the formation of mixtures of complexes **1a** and **3a.** After the mixture solution was stirred overnight, IR ν_{NO} spectrum displaying two strong stretching bands at 1675 s, 1658 s cm^{-1} indicated the formation of complex **2a-PPN**. The dark-green solution was dried under vacuum and redissovled in THF-diethyl ether. The dark-green solution was then filtered through Celite, and hexane was added into the filtrate to precipitate the deep green solid complex **2a-PPN** (yield 0.070 g, 78%) characterized by FTIR and UV−vis.

Reaction of Complex 2a-PPN and [PPN][SEt]. To the CH_3CN solution of complex **2a-PPN** (0.089 g, 0.1 mmol) was added in a

(20) (a) Pellat, J.-C.; Henry, Y. *J. Biol. Chem.* **1991**, *266*, 10162–10167. (b) Lancaster, J. R.; Hibbs, J. B. *Proc. Natl. Acad. Sci. U. S. A.* **1990**, *87*, 1223–1227. (c) Lee, M.; Arosio, P.; Cozzi, A.; Chasteen, N. D. *Biochemistry* **1994**, *33*, 3679–3687.

(21) Chong, D.; Georgakaki, I. P.; Mejia-Rodriguez, R.; Sanabria-Chinchilla, J.; Soriaga, M. P.; Darensbourg, M. Y. *Dalton Trans.* **2003**, 4158–4163.

dropwise manner the CH_3CN solution of [PPN][SEt] (0.120 g, 0.2 mmol) at ambient temperature. The reaction was monitored by FTIR. After the reaction solution was stirred at room temperature for 10 min, the IR ν_{NO} spectrum shows absorption bands at 1722 s, 1678 s, 1658 s, 1625 m, 1580 sh cm^{-1} indicating the formation of complexes **2a-PPN**, **3a**, and, presumably, the thermally unstable $[(EtS)_2Fe(NO)_2]^{2-}$. The reaction solution was stirred for another 2 h, and the same absorption bands (1722 s, 1678 s, 1658 s, 1625 m, 1580 sh cm^{-1}) were observed. Another two equivalents of [PPN][SEt] (0.120 g, 0.2 mmol) were then added to the above mixture solution and stirred for 20 min. The IR ν_{NO} spectrum changing from absorption bands (1722 s, 1678 s, 1658 s, 1625 m, 1580 sh cm^{-1}) to (1722 s, 1680 s, 1625 m, 1580 sh cm^{-1}) suggested the formation of complex **3a** and the proposed $[(EtS)_2Fe(NO)_2]^{2-}$. The solvent was removed under vacuum. The crude solid was redissolved in THF-diethyl ether and filtered through Celite to remove the insoluble [PPN][SEt]. Addition of hexane into the filtrate led to the precipitation of brown solid **3a** (yield 0.040 g, 26%) identified by IR and UV−vis.

Transformation of Complex 3a into Complex 2a-PPN in CH_3CN. Complex **3a** (0.155 g, 0.2 mmol) was dissolved in CH_3CN (20 mL), and the degradation of CH_3CN solution of complex **3a** was monitored by FTIR immediately. The IR ν_{NO} spectrum of the solution showing two strong absorption bands at 1722 s, 1680 s cm^{-1} indicated the existence of complex **3a**. The transformation of complex **3a** in CH_3CN under N_2 was monitored by FTIR. After the solution was stirred at 50 °C for 1 h, the IR ν_{NO} stretching frequencies at 1722 s, 1680 s, 1658 m cm^{-1} implicated the formation of mixtures of complexes **2a-PPN** and **3a**. The solution was then kept stirring at 50 °C for a week. The IR ν_{NO} spectrum displayed two absorption bands at 1675 s, 1658 s cm^{-1} assigned to the formation of complex **2a-PPN**. The dark-green solution was dried under vacuum and then redissolved in THF-diethyl ether. The dark-green solution was then filtered through Celite, and addition of hexane into the filtrate led to the precipitation of deep green solid **2a-PPN** (yield 0.063 g, 71%) characterized by FTIR and UV−vis.

Transformation of Complex 3a into Complexes 1a and 2a-PPN in CH_2Cl_2. Complex **3a** (0.155 g, 0.2 mmol) was dissolved in CH_2Cl_2 (20 mL) under N_2 at ambient temperature and monitored by FTIR immediately. The IR ν_{NO} spectrum of the solution showing absorption bands at 1809 vw, 1775 m, 1749 sh, 1732 s, 1684 s cm^{-1} indicated the formation of complexes **1a** and **3a.** After the mixture solution was stirred at ambient temperature for 2 h, the IR ν_{NO} spectrum displayed five absorption bands at 1809 vw, 1775 s, 1749 s, 1674 s, 1654 s cm^{-1} assigned to the formation of complexes **1a** and **2a-PPN**. The yellow green solution was dried under vacuum and redissolved in THF-diethyl ether. The yellow green solution was then filtered through Celite to remove the insoluble solid. Hexane was added to the filtrate to separate the deep green precipitate complex **2a-PPN** (yield 0.031 g, 35%) identified by FTIR/UV−vis, and the orange red solution. The orange red solution was dried under vacuum to obtain the semi-oily product complex **1a** characterized by FTIR, ^1H NMR and UV−vis. Complex **1a** was recrystallized with MeOH at −20 °C to obtain the deep brown crystals (yield 0.007 g, 20%).

Transformation of Complex 3b in CH_3CN. Complex **3b** (0.058 g, 0.1 mmol) was dissolved in 5 mL CH_3CN, and the solution was immediately monitored by FTIR. The IR ν_{NO} spectrum of the solution showing two absorption bands at 1718 s, 1675 s cm^{-1} indicated the existence of complex **3b**. After the solution was stirred at ambient temperature for 30 h, the absorption bands at 1807 vw, 1773 s, 1745 s, 1718 s, 1671 s, 1653 s cm^{-1} implicated the formation of complexes **3b**, $[Fe(\mu\text{-}S^tBu)(NO)_2]_2$ (**1b**), and [Na-18-crown-6-ether][$Fe(\mu\text{-}S^tBu)(NO)_2]_2$ (**2b**). The mixture solution was then kept stirring at room temperature for 96 h, and the IR ν_{NO} spectrum displayed two absorption bands at 1671 s, 1652 s cm^{-1} assigned to complex **2b**. The solvent was removed under vacuum and then washed with diethyl ether. The isolated crude solid was redissolved in THF-diethyl ether and filtered through Celite. Addition of hexane into the filtrate led to the precipitation of the dark green solid **2b** (yield 0.028 g, 80%) characterized by IR and UV−vis. IR ν_{NO}: 1670 s, 1650 s cm^{-1} (CH_2Cl_2); 1672 s, 1652 s cm^{-1} (CH_3CN). Absorption spectrum (THF) [λ_{max}, nm (ε, M^{-1} cm^{-1})]: 310 (7300), 435 (4250), 639 (1900), 982 (3100).

Transformation of Complex 3b in CH_2Cl_2. Complex **3b** (0.058 g, 0.1 mmol) was loaded into a 20 mL Schlenk tube, and 10 mL of CH_2Cl_2 was added via cannula under positive N_2. The solution was stirred at ambient temperature for 20 min, and the IR ν_{NO} spectrum displayed three absorption bands at 1806 vw, 1771 s, 1744 s cm^{-1} assigned to the formation of complex **1b**. The solvent was removed under vacuum. The isolated crude solid was redissolved in diethyl ether (5 mL) and filtered through Celite to remove the insoluble solid. The volume of the solution was then concentrated to 0.5 mL under vacuum, and CH_3CN (4 mL) was added. The CH_3CN-diethyl ether solution of complex **1b** was kept in the refrigerator at −20 °C overnight, and the pure solid complex **1b** was collected by filtration (yield 0.012 g, 60%).

Reaction of Complex 1b and 2 equiv of [Na-18-crown-6-ether][S^tBu]. To the CH_3CN suspension solution of complex **1b** (0.041 g, 0.1 mmol) was added in a dropwise manner the CH_3CN solution of [Na-18-crown-6-ether][S^tBu] (0.068 g, 0.2 mmol) at 0 °C. The reaction was monitored by FTIR. After the mixture solution was stirred at 0 °C for 10 min, the IR ν_{NO} spectrum showed absorption bands at 1807 vw, 1773 s, 1746 s, 1718 s, 1672 s, 1653 s cm^{-1} indicating the formation of complexes **1b**, **2b**, and **3b**.[13] The reaction solution was further stirred at room temperature for 2 h, and the same absorption bands (1807 vw, 1773 s, 1746 s, 1718 s, 1672 s, 1653 s cm^{-1}) were observed. The mixture solution was then kept stirring at room temperature for 96 h, and the IR ν_{NO} spectrum displayed two absorption bands at 1671 s, 1652 s cm^{-1}, assigned to the complete formation of complex **2b**. The solvent was removed under vacuum and then washed with diethyl ether. The isolated dark green crude solid was redissolved in THF-diethyl ether and filtered through Celite. Addition of hexane into the filtrate led to the precipitation of the dark green solid **2b** (yield 0.060 g, 85%) characterized by IR and UV−vis.[13]

EPR Measurements. EPR measurements were performed at X-band using a Bruker EMX spectrometer equipped with a Bruker TE102 cavity. The microwave frequency was measured with a Hewlett-Packard 5246L electronic counter. At 298 K, X-band EPR spectrum of complex **2a-PPN** in THF was obtained with a microwave power of 20.020 mW, frequency at 9.604 GHz, and modulation amplitude of 0.8 G at 100 KHz. At 77 K, X-band EPR spectrum of complex **2a-PPN** frozen in THF was obtained with a microwave power of 19.971 mW, frequency at 9.485 GHz, and modulation amplitude of 0.8 G at 100 KHz. At 298 K, X-band EPR spectra of complex **3a** in MeOH were obtained with a microwave power of 5.016 mW, frequency at 9.633 GHz, and modulation amplitude of 0.8 G at 100 KHz.

Magnetic Measurements. The magnetic data were recorded on a SQUID magnetometer (MPMS5 Quantum Design Company) under 0.5 T external magnetic field in the temperature range of 2−300 K. The magnetic susceptibility data were corrected with temperature independent paramagnetism (TIP, 2×10^{-4} cm^3 mol^{-1}) and ligands' diamagnetism by the tabulated Pascal's constants.

X-ray Absorption Measurements. All X-ray absorption experiments were carried out at the National Synchrotron Radiation Research Center (NSRRC), Hsinchu, Taiwan. Both Fe K-edge and L-edge were recorded at room temperature. For Fe K-edge measurements, the experiment were performed in transmission mode at the BL-17C X-ray Wiggler beamline with a double crystal Si(111) monochromator. The energy resolution $\Delta E/E$ was estimated to be about 2×10^{-4}. High harmonics were rejected by Rh-coated mirrors. The spectra were scanned from 6.912 to 8.004 KeV using a gas-ionization detector. A reference Fe foil is always used simultaneously for the calibration of photon energy. The ion chambers used to measure the incident (I_0) and transmitted (I) photon intensities were filled with a mixture of N_2 and He gases and a mixture of N_2 and Ar gases, respectively.

For Fe L-edge measurements, the data were collected at the 6-m high-energy spherical grating monochromator (HSGM) beamline with 10 μm opening slits, corresponding to ~0.15 eV energy resolution for the Fe L-edge energy range. All samples were ground to powder from single crystals, stuck to conducting tape, and then subjected to an ultrahigh vacuum chamber (10^{-9} torr). The absorption spectra were recorded in total electron yield mode by measuring the sample drain current. Each spectrum was calibrated by using the known Fe L_{III} edge absorption peak at 708.5 eV of Fe_2O_3.

MO Calculation. DFT calculations are carried out with the Amsterdam Density Functional 2006.01 (ADF)[22] with the generalized gradient approximation (GGA). The corrections of LDA and GGA parts are taken from VWN[23] and BP.[24,25] The SCALAR ZORA is used for relativistic corrections. The excitation energies were calculated using TDDFT. The static DFT calculations were performed as starting points for the TDDFT calculations. The time-dependent portion of the calculations utilized the functional given by the adiabatic linear density approximation (ALDA). The triple-ζ Slater type function complemented with two polarization functions (TZ2P) are used for all atoms. Unrestricted open shell MO calculations of complex **2a** has been computed with and without geometric coordinates optimization. In the single point calculation, the molecular symmetry is kept to C_i, which is the same as the original symmetry adapted from the crystal structure. In geometric optimization, both C_i and the broken symmetry state C_1 are computed. The optimization criteria are as follows: (i) the difference in the total energy between two successive cycles has to be less than 0.001 hartree; (ii) the maximal difference in the norm of the gradient between two successive cycles has to be less than 0.01 hartree/Å; (iii) the maximal difference in the Cartesian coordinate between two successive cycles has to be less than 0.01 Å. However, both states give very close results with maximum differences of about 0.006 Å in bond distance and about 0.01 eV in total energy. A comparison between with and without geometric optimization at C_i symmetry indicates that both states have similar MO coefficients except the one closer to the first absorption peak is at the optimized geometry in the TDDFT calculation. Therefore, the data reported in this paper are based on the optimized C_i symmetry results. The coordinate system employed is such that the origin is set at the center of the Fe(1)−S(1)−Fe(1A)−S(1A) plane; the x-axis is collinear with the Fe(1)−Fe(1A) direction; the y-axis is perpendicular to x-axis and in the direction of center to S(1).

Crystallography. Crystallographic data and structure refinements parameters of complexes **1a**, **2a-PPN**, **2a-Na**, and **2a-Me$_4$N** are summarized in the Supporting Information. The crystals chosen for the X-ray diffraction studies measured $0.30 \times 0.20 \times 0.10$ mm for complex **1a**, $0.8 \times 0.7 \times 0.5$ mm for complex **2a-PPN**, $0.31 \times 0.26 \times 0.1$ mm for complex **2a-Na**, and $0.45 \times 0.4 \times 0.2$ mm for complex **2a-Me$_4$N**, respectively. Each crystal was mounted on a glass fiber and quickly coated in epoxy resin. Unit-cell parameters were obtained by least-squares refinement. Diffraction measurements for complexes **1a**, **2a-PPN**, **2a-Na**, and **2a-Me$_4$N** were carried out on a SMART Apex CCD diffractometer with graphite-monochromated Mo Kα radiation ($\lambda = 0.7107$ Å) and between 3.20° and 28.30° for complex **1a**, between 2.11° and 25.68° for complex **2a-PPN**, between 2.26° and 25.34° for complex **2a-Na**, and between 2.35° and 25.34° for complex **2a-Me$_4$N**. Least-squares refinement of the positional and anisotropic thermal parameters of all non-hydrogen atoms and fixed hydrogen atoms was based on F^2. A SADABS[26] absorption correction was made. The SHELXTL[27] structure refinement program was employed.

Acknowledgment. We gratefully acknowledge financial support from the National Science Council of Taiwan.

Supporting Information Available: X-ray crystallographic files in CIF format for the structure determinations of [Fe(μ-SEt)(NO)$_2$]$_2$, [PPN][Fe(μ-SEt)(NO)$_2$]$_2$, [Na-18-Crown-6][Fe(μ-SEt)(NO)$_2$]$_2$ and [Me$_4$N][Fe(μ-SEt)(NO)$_2$]$_2$. This material is available free of charge via the Internet at http://pubs.acs.org.

IC800360M

(22) (a) teVelde, G.; Bickelhaupt, F. M.; van Gisbergen, S. J. A.; Guerra, C. F.; Baerends, E. J.; Snijders, J. G.; Ziegler, T. *J. Comput. Chem.* **2001**, *22*, 931–967. (b) Fonseca Guerra, C.; Snijders, J. G.; teVelde, G.; Baerends, E. J. *Theor. Chem. Acc.* **1998**, *99*, 391–403. (c) van Gisbergen, S. J. A.; Snijders, J. G.; Baerends, E. J. *Comput. Phys. Commun.* **1999**, *118*, 119–138. (d) van Gisbergen, S. J. A.; Snijders, J. G.; Baerends, E. J. *J. Chem. Phys. Commun.* **1995**, *103*, 9347–9354.
(23) Vosko, S. H.; Wilk, L.; Nusair, M. *Can. J. Phys.* **1980**, *58*, 1200–1211.
(24) Becke, A. D. *Phys. Rev. A* **1988**, *38*, 3098–3100.
(25) Perdew, J. P.; Yang, W. *Phys. Rev. B* **1986**, *33*, 8800–8802.
(26) Sheldrick, G. M. *SADABS, Siemens Area Detector Absorption Correction Program*; University of Göttingen: Germany, 1996.
(27) Sheldrick, G. M. *SHELXTL, Program for Crystal Structure Determination*; Siemens Analytical X-ray Instruments Inc.: Madison, WI, 1994.